Nuclear pair electron spin echo envelope modulation

Author(s):
Jeschke, Gunnar

Publication date:
2023-06

Permanent link:
https://doi.org/10.3929/ethz-b-000623152

Originally published in:
Journal of Magnetic Resonance Open 14-15, https://doi.org/10.1016/j.jmro.2023.100094

Journal of Magnetic Resonance Open 14-15 (2023) 100094

Contents lists available at ScienceDirect

Journal of Magnetic Resonance Open

journal homepage: www.sciencedirect.com/journal/journal-of-magnetic-resonance-open

Research article

Nuclear pair electron spin echo envelope modulation

G. Jeschke

ETH Zürich, Vladimir-Prelog-Weg 2, Zürich, 8093, Switzerland

ARTICLE INFO

Dataset link: 10.5281/zenodo.7383253

Keywords:
Relaxation
Decoherence
Spin diffusion
Nuclear spin bath
Dynamical decoupling
Noise spectroscopy

ABSTRACT

The interaction of electron spins with homonuclear spin pairs in their vicinity is one of the dominating mechanisms of electron spin echo decay at low temperature and low concentration. Here, we study this mechanism using established concepts of electron spin echo envelope modulation (ESEEM). We obtain analytical expressions for the Hahn echo, the refocused echo, the stimulated echo, and Carr–Purcell pulse trains with small numbers of π pulses. Hahn echo decay is well approximated by the product of nuclear pair ESEEM functions. The same approximation can explain dependence of stimulated echo decay on the first interpulse delay and provides reasonable time scale estimates for decay of Carr–Purcell echos after an odd number of π pulses. Carr–Purcell echoes after an even number of π pulses are rather sensitive to correlations within larger nuclear spin clusters. Approximations improve for both odd and even numbers of π pulses by factorising the nuclear spin bath into disjoint clusters, provided that modulation due to pairs of spins belonging to different clusters is considered in addition to cluster modulation. The analytical ESEEM expressions for the Hahn echo and the Carr–Purcell echo after two π pulses have the same mathematical form as the filter functions of these sequences of spin noise spectroscopy. This coincidence provides a computationally very efficient way of predicting Hahn echo decay induced by homonuclear spin pairs. The analytical pair product approximation predicts the previously observed (Bahrenberg et al., 2021) increase of the refocused echo amplitude when one refocusing time is incremented and other one is fixed but longer. In contrast, the spin-noise concept fails to predict this effect.

1. Introduction

Electron spin typically resides in a bath of nuclear spins. It is known since a long time that this hyperfine-coupled nuclear spin bath governs decay of the two-pulse (Hahn) echo at low electron spin concentration and sufficiently low temperatures [1]. Early experiments demonstrated that stimulated echo decay is influenced by the nuclear spin bath as well [2]. Careful experimental studies established that, for nitroxides in glassy solvents at temperatures between 11 and 40 K, echo decay is dominated by matrix protons, with distinct behaviour of methyl protons [3]. A spin diffusion barrier had been assumed to prevent protons very close to the electron spin to contribute to decay [4]. Electron spin memory loss to the nuclear spin bath attracted renewed interest in the context of quantum information processing where it was termed decoherence [5,6]. Based on an understanding of decoherence as spectral-diffusion induced, prolongation of the decoherence time was achieved by multi-pulse Carr–Purcell sequences [7]. Such prolongation of electron spin phase memory was termed dynamical decoupling [8]. Microscopically, the decoherence is induced by flip-flops of nuclear spin pairs that are in turn driven by dipole–dipole coupling between nuclear spins. The terms of the spin Hamiltonian responsible for these flip-flops act on the zero-quantum transitions of the pairs in the nuclear Zeeman basis. If a nuclear spin is involved in two spin pairs, the two flip-flop terms involving this spin do not commute, which renders an exact treatment of nuclear bath-induced decoherence (NBID) unfeasible.

Approximate quantitative descriptions of NBID were developed in terms of cluster expansion [6], linked-cluster expansion [9] and cluster-correlation expansion (CCE) [10–12]. Alternatively, the effect of the nuclear spin bath can be understood in terms of nuclear spin noise. In this picture, dynamical decoupling is explained by multi-pulse sequences acting as filters on the spectral density function of this noise [13,14]. By reversing this idea, echo decay curves obtained with multi-pulse sequences can be used to reconstruct the spectral density function in an approach called noise spectroscopy [15–18]. The two pictures were connected by deriving a description of the NIBD process in terms of Gaussian spin noise from cluster expansion [19]. Recently, a contribution to background decay in the constant-time six-pulse relaxation-induced dipolar modulation enhancement (RIDME) experiment was traced back to interaction of the electron spin with the nuclear spin bath as well [20]. This decay contribution could be modelled by a diffusion equation based on a picture of longitudinal spectral diffusion induced by nuclear pair flip-flops [21].

E-mail address: gjeschke@ethz.ch.

https://doi.org/10.1016/j.jmro.2023.100094
Received 30 November 2022; Received in revised form 9 January 2023; Accepted 14 January 2023
Available online 20 January 2023

The understanding obtained by the quantum-information processing community was taken up by the electron paramagnetic resonance (EPR) community with the aims of characterising decoherence in glassy solids and improving resolution of pulsed EPR experiments by dynamical decoupling [22–30]. Two of the first three studies that applied CCE to dense proton systems found that expansion up to order two, i.e. up to only pairs, provided surprisingly good predictions [24,25]. On the other hand, a study of refocused echo decay revealed that echo amplitude is not a monotonous function of total evolution time for this pulse sequence [28]. This finding indicates that NBID can be refocused rather than merely suppressed, a fact that is at odds with a spin noise picture.

Here we try to gain a better understanding based on the fact that CCE up to second order can be viewed as a factorisation of the decay function into nuclear pair contributions. For nuclear pairs, analytical expressions can be obtained, as has already been established for the case of the Hahn echo [6]. We note that such expressions can be conveniently derived by product operator formalism [31] in analogy to the case of electron spin echo envelope modulation (ESEEM) due to a single nuclear spin 1/2 [32]. The nuclear pair ESEEM picture provides insight into the microscopic mechanism of dynamical decoupling and into the relation between the decays of the Hahn echo and the stimulated echo. The analytical expressions allow for computationally efficient simulation of decay curves. They provide a reasonable approximation of dynamical decoupling efficiency for Carr–Purcell sequences with an odd number of π pulses, whereas they overestimate efficiency of dynamical decoupling for an even number of π pulses.

This paper is structured as follows. First, we provide a product operator formalism framework for deriving analytical expressions for nuclear pair ESEEM for arbitrary pulse sequences. Second, we discuss dynamical decoupling on the example of a Carr–Purcell sequence with two π pulses. We further consider frequencies and modulation depths of nuclear pair ESEEM in Carr–Purcell sequences with up to four π pulses. To this end, we compare experimental data from previous work [27] with numerical simulations based on our analytical expressions and a model for the water–glycerol glass. We consider limitations of describing decoherence during multipulse-sequences by a product of nuclear pair ESEEM functions and introduce cluster factorisation as a computationally efficient way of improving on the pair product approximation. Third, we consider stimulated echo decay in the nuclear pair ESEEM picture and compare experimental results with simulations. Fourth, we discuss the relation between the pictures of coherent nuclear pair ESEEM and of stochastic spectral diffusion. Fifth, we relate nuclear pair ESEEM to a spectral density function of spin noise for the Hahn echo and the Carr–Purcell sequence with two refocusing pulses. Sixth, we show that the recently observed increase of refocused echo amplitude with increasing pulse sequence duration [28] is a consequence of refocusing of nuclear pair ESSEM. We conclude by considering questions that remain open.

2. Theory

The simplest spin system for studying NBID consists of one electron spin $S = 1/2$ and two nuclear spins $I_1 = 1/2$ and $I_2 = 1/2$. We formulate the spin Hamiltonian in the rotating frame for the electron spin and the laboratory frame for the two nuclear spins and express it in angular frequency units,

$$\begin{aligned}\hat{\mathcal{H}} &= \Omega_S \hat{S}_z + \omega_I \left(\hat{I}_{1,z} + \hat{I}_{2,z}\right) \\ &\quad + A_1 \hat{S}_z \hat{I}_{1,z} + A_2 \hat{S}_z \hat{I}_{2,z} \\ &\quad + \omega_{\mathrm{nn}} \left[\hat{I}_{1,z}\hat{I}_{2,z} - \frac{1}{4}\left(\hat{I}_1^+ \hat{I}_2^- + \hat{I}_1^- \hat{I}_2^+\right)\right] , \end{aligned} \tag{1}$$

Herein, we have neglected the pseudo-secular part of the hyperfine coupling thus excluding single-nucleus ESEEM. As pointed out by an anonymous reviewer, the shift of nuclear frequencies by this contribution can potentially lead to a situation where nuclear frequencies become near-degenerate in one of the electron spin manifolds, but not in the other one. For such nuclear spin pairs, neglect of the pseudo-secular coupling would substantially influence the predicted contribution to electron spin decoherence. The case is beyond the scope of the present paper and will be considered elsewhere. The nuclear dipole–dipole coupling

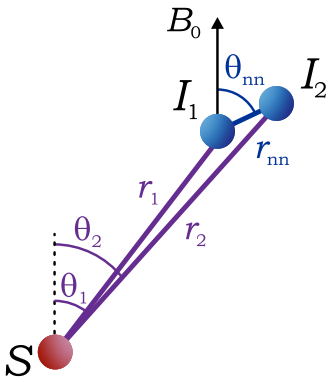

Fig. 1. Geometry of the system consisting of one electron spin $S = 1/2$ (red) and two nuclear spins $I_1 = 1/2$ and $I_2 = 1/2$ (blue). The vertical arrow denotes the magnetic field B_0. (For interpretation of the references to colour in this figure legend, the reader is referred to the web version of this article.)

$$\omega_{\mathrm{nn}} = \frac{\mu_0 \hbar \gamma_I^2}{4\pi r_{nn}^3}\left(1 - 3\cos^2\theta_{\mathrm{nn}}\right) \tag{2}$$

and through-space secular hyperfine couplings

$$A_i = \frac{\mu_0 \hbar \gamma_I \gamma_S}{4\pi r_i^3}\left(1 - 3\cos^2\theta_i\right) \tag{3}$$

depend on geometry of the nuclear spin pair with respect to the magnetic field and to the electron spin as shown in Fig. 1. We neglect chemical shift and nuclear J-coupling, which are much smaller than the nuclear dipole–dipole coupling.

The nuclear flip-flop operators $\hat{I}_1^+\hat{I}_2^- + \hat{I}_1^-\hat{I}_2^+$ contribute the only off-diagonal term. Since they do not connect the subspaces corresponding to the α and β state of the electron spin, these subspaces can be diagonalised separately by the transformations

$$\begin{aligned} T^\alpha &= \exp\left\{-i\eta\hat{S}^\alpha\left(\hat{I}_{1,y}\hat{I}_{2,x} - \hat{I}_{1,x}\hat{I}_{2,y}\right)\right\} \\ T^\beta &= \exp\left\{-i\eta\hat{S}^\beta\left(\hat{I}_{1,y}\hat{I}_{2,x} - \hat{I}_{1,x}\hat{I}_{2,y}\right)\right\} . \end{aligned} \tag{4}$$

The rotation angle η is visualised in Fig. 2(a) and given by

$$\eta = \arctan\frac{\omega_{\mathrm{nn}}}{A_1 - A_2} . \tag{5}$$

The nuclear zero-quantum frequency in the eigenbasis evaluates to

$$\omega_{\mathrm{nZQ}} = \frac{1}{2}\sqrt{(A_1 - A_2)^2 + \omega_{\mathrm{nn}}^2} , \tag{6}$$

The two subspace transformations commute. Thus, they can be combined into

$$\hat{T}_{\mathrm{EB}} = 2\eta\hat{S}_z\hat{I}_{1,y}\hat{I}_{2,x} - 2\eta\hat{S}_z\hat{I}_{1,x}\hat{I}_{2,y} . \tag{7}$$

In its eigenbasis, the Hamiltonian takes the form

$$\begin{aligned}\hat{\mathcal{H}}_{\mathrm{EB}} &= \Omega_S\hat{S}_z + \omega_I\left(\hat{I}_{1,z} + \hat{I}_{2,z}\right) \\ &\quad + A_1'\hat{S}_z\hat{I}_{1,z} + A_2'\hat{S}_z\hat{I}_{2,z} \\ &\quad + \omega_{\mathrm{nn}}\hat{I}_{1,z}\hat{I}_{2,z} , \end{aligned} \tag{8}$$

with the effective hyperfine couplings

$$A_{1,2}' = \frac{A_1 + A_2}{2} \pm \omega_{\mathrm{nZQ}} . \tag{9}$$

By transforming the electron-spin excitation operator $\hat{S}_x$ into the eigenbasis,

$$\hat{S}_x \xrightarrow{\hat{T}_{\mathrm{EB}}} \cos^2\left(\frac{\eta}{2}\right)\hat{S}_x +$$

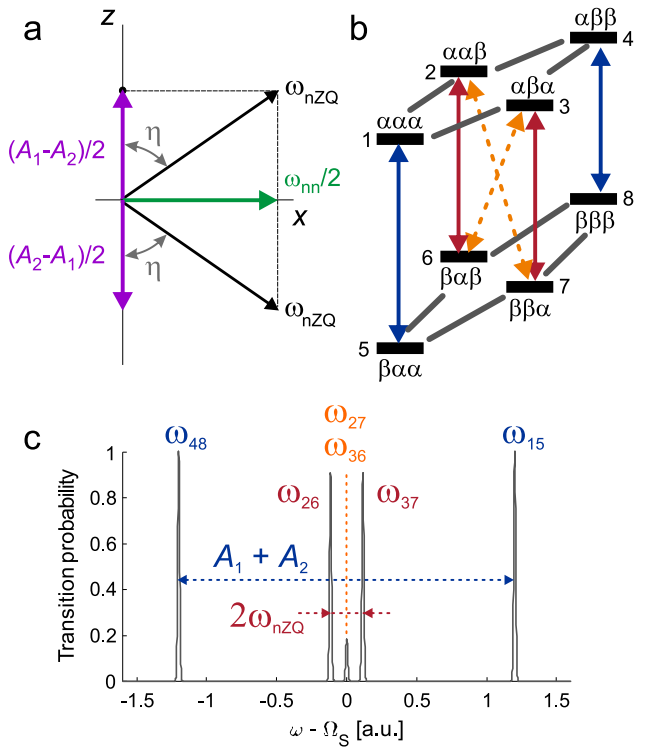

Fig. 2. Diagonalisation of the Hamiltonian (a) Subspace rotations by angle η in counterclockwise direction in the electron spin α subspace and in clockwise direction in the β subspace diagonalise the Hamiltonian. The effective nuclear zero-quantum frequencies have the same absolute value ω_{nZQ}. (b) The two nominally forbidden transitions $\beta\alpha\beta \leftrightarrow \alpha\beta\alpha$ and $\beta\beta\alpha \leftrightarrow \alpha\alpha\beta$ (orange) become partially allowed, while transition moment of the nominally allowed transitions $\beta\alpha\beta \leftrightarrow \alpha\alpha\beta$ and $\beta\beta\alpha \leftrightarrow \alpha\beta\alpha$ (red) is somewhat reduced. The transitions $\beta\alpha\alpha \leftrightarrow \alpha\alpha\alpha$ and $\beta\beta\beta \leftrightarrow \alpha\beta\beta$ (blue) remain unaffected. (c) In the EPR spectrum, frequencies and amplitudes change for the inner two lines of the hyperfine quartet (red labels). The forbidden transitions appear at the unperturbed electron Zeeman frequency. (For interpretation of the references to colour in this figure legend, the reader is referred to the web version of this article.)

$$4\cos\left(\frac{\eta}{2}\right)\sin\left(\frac{\eta}{2}\right) \times\left(\hat{S}_y\hat{I}_{1,y}\hat{I}_{2,x} - \hat{S}_y\hat{I}_{1,y}\hat{I}_{2,x}\right) + 4\sin^2\left(\frac{\eta}{2}\right)\hat{S}_x\hat{I}_{1,z}\hat{I}_{2,z}\,, \tag{10}$$

and expanding the result into single-transition operators, we find that the transition moment of the $\beta\alpha\alpha \leftrightarrow \alpha\alpha\alpha$ and $\beta\beta\beta \leftrightarrow \alpha\beta\beta$ transitions (coloured blue in Fig. 2(b)) remains unity, the one of the $\beta\alpha\beta \leftrightarrow \alpha\alpha\beta$ and $\beta\beta\alpha \leftrightarrow \alpha\beta\alpha$ transitions (red) becomes $\cos\eta$, and the one of the $\beta\alpha\beta \leftrightarrow \alpha\beta\alpha$ and $\beta\beta\alpha \leftrightarrow \alpha\alpha\beta$ transitions (orange) becomes $\sin\eta$. This situation is analogous to the one encountered in single-nucleus ESEEM experiments [32] with the exceptions that in the pair case the angles for the two subspace rotations are equal, the nuclear frequencies in the two subspaces are equal, and the transition moments and nuclear frequencies do not depend on magnetic field.

In the formally forbidden transitions with transition moment $\sin\eta$ all three spins change their state. This exactly cancels all spin–spin interactions in the system. Hence, these transitions occur at the electron Zeeman frequency, i.e. at the resonance offset Ω_S in the rotating frame (Fig. 2(c)). The formally forbidden transitions with transition moment $\cos\eta$ appear at frequencies $\Omega_S \pm \omega_{nZQ}$.

3. Hahn echo decay

We are now in a position to compute an analytical formula for nuclear pair two-pulse ESSEM by product operator formalism. As a time variable we use the total length T of the pulse sequence (Fig. 3(a) with

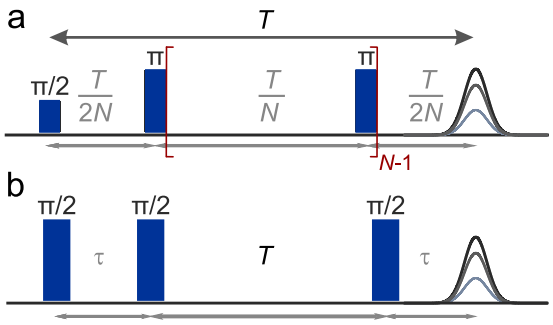

Fig. 3. Definition of time variables in the considered pulse sequences (a) Hahn echo ($N = 1$ and Carr–Purcell sequences ($N = 2 \ldots 5$) with total length T. (b) Stimulated echo sequence with preparation time τ and evolution time T.

$N = 1$). The analytical expression for the spin density operator σ_{det} at the time of detection follows from the thermal equilibrium spin density operator $-\hat{S}_z$ by the following sequence of transformations

$$-\hat{S}_z \xrightarrow{\pi/2\hat{S}_x} \xrightarrow{\hat{T}_{EB}} \xrightarrow{\hat{H}_{EB}T/2} \xrightarrow{-\hat{T}_{EB}} \xrightarrow{\pi\hat{S}_x} \xrightarrow{\hat{T}_{EB}} \ldots \xrightarrow{\hat{H}_{EB}T/2} \xrightarrow{-\hat{T}_{EB}} \sigma_{det}\,, \tag{11}$$

The echo refocuses along the $-y$ direction. Hence, the echo amplitude $W(T)$ is the negative coefficient of $\hat{S}_y$ in the expression for σ_{det}. We find

$$W(T) = 1 - \frac{3}{2}\lambda - \frac{1}{2}\lambda\cos\left(\omega_{nZQ}T\right) + 2\lambda\cos\left(\frac{1}{2}\omega_{nZQ}T\right) \tag{12}$$

with the modulation depth

$$\lambda = \sin^2\eta\cos^2\eta = \frac{\left(A_1 - A_2\right)^2\omega_{nn}^2}{\left[\left(A_1 - A_2\right)^2 + \omega_{nn}^2\right]^2} = \frac{\left(A_1 - A_2\right)^2\omega_{nn}^2}{16\omega_{nZQ}^4}\,. \tag{13}$$

We have checked (see Supporting Information Section S1) that Eq. (12) is equivalent to the analytical solution for pairs reported in [6].

As expected, the modulation vanishes when the nuclear dipole–dipole coupling vanishes ($\omega_{nn} = 0$). It also vanishes when the hyperfine coupling to both nuclei is the same ($A_1 = A_2$). In this case, nuclear spin flip-flops do not induce any local field change at the electron spin. The modulation depth attains a maximum of 1/4 at the field-independent matching condition

$$|A_1 - A_2| = |\omega_{nn}|\,. \tag{14}$$

Eq. (12) has another interesting property. For small $\omega_{nZQ}T$, where the approximation $\cos(\omega_{nZQ}T) \approx 1 - \omega_{nZQ}^2T^2/2$ holds, one has $W(T) \approx 1$. Hence, the leading term in a Taylor expansion of the right-hand side of Eq. (12) is of the fourth power in T and ω_{nZQ}. For $\omega_{nZQ}T \ll 1$ we find

$$W(T) \approx 1 - \frac{\lambda}{64}\left(\omega_{nZQ}T\right)^4 \approx 1 - \frac{\left(A_1 - A_2\right)^2\omega_{nn}^2T^4}{1024}\,. \tag{15}$$

As in the case of single-nucleus two-pulse ESEEM [33], echo modulation can be understood in terms of coherence transfer echoes. Such echoes arise because the π pulse transfers coherence between two electron-spin transitions. The frequency difference between these two transitions is then not refocused and appears as a modulation frequency. In the case at hand, coherence on the fully allowed transitions (blue in Fig. 2(b,c)) is simply refocused and not transferred to other transitions. Coherence on the slightly disallowed (red) and slightly

allowed (orange) transitions undergoes branching to other transitions during the π pulse. It is clear from Fig. 2(c) that four pairs of transitions $(\omega_{26},\omega_{27})$, $(\omega_{26},\omega_{36})$, $(\omega_{37},\omega_{27})$, and $(\omega_{37},\omega_{36})$ cause phase gain with frequency ω_{nZQ} after branching whereas only pair $(\omega_{26},\omega_{37})$ causes phase gain with frequency $2\omega_{\mathrm{nZQ}}$. Since the phase gain arises only in the interval of length $T/2$ between the π pulse and echo formation, the modulation frequencies with respect to total length T of the pulse sequence are only half as large.

As a microscopic echo decay mechanism, such nuclear pair ESEEM is at odds with descriptions were the frequency changes occur by nuclear flip-flops at random times during free evolution. In fact, the frequency changes are induced exclusively by the π pulses. We shall discuss below why descriptions that assume flip-flops at random times can still be successful.

For single-nucleus ESEEM, the signal for a system with n nuclei is given by the product $\prod_{i=1}^{n} W_i$, where the W_i are the signals for a single nucleus [32]. In the absence of couplings between nuclear spins this product rule would be exact. This is because single-nucleus ESEEM is generated by pseudo-secular terms in the spin Hamiltonian of the form $B_i\hat{S}_z\hat{I}_{i,x}$, which pairwise commute ($[\hat{S}_z\hat{I}_{i,x},\hat{S}_z\hat{I}_{j,x}]=0$). In contrast, the pseudo-secular terms of the form $\hat{I}_i^+\hat{I}_j^- + \hat{I}_i^-\hat{I}_j^+$ in nuclear pair ESEEM do not commute for two pairs that share one nucleus. Hence, a product rule does not strictly apply. However, in cases where CCE up to order two is a good approximation [24,25,30], the product of nuclear pair ESEEM signals is a good approximation as well. We consider all pairs of nuclei and index them by p. Note that each nucleus belongs to many pairs. Since single nuclei do not contribute to decay according to the Hamiltonian given in Eq. (1), consideration of all these pairs does not cause double counting. We can thus write for the Hahn echo decay due to the nuclear spin bath in the analytical pair product approximation (APPA)

$$W(T) \approx \prod_p W_p(T) \approx \prod_p \left[1 - 4\lambda_p \cos^4\left(\frac{\omega_{\mathrm{nZQ},p}T}{4}\right)\right], \quad (16)$$

where we have rewritten the cosine terms in a shorter form. Because all the individual $\lambda_p \cos^4\left(\omega_{\mathrm{nZQ},p}T/4\right)$ are much smaller than unity, we can write as an approximation of virtually the same quality

$$\ln W(T) \approx -4\sum_p \lambda_p \cos^4\left(\frac{\omega_{\mathrm{nZQ},p}T}{4}\right). \quad (17)$$

We have tested this proposition on existing Hahn echo decay data [27] for the nitroxide radical D-mNOPEG in natural isotope abundance water/glycerol glass (1:1 v/v) acquired at a concentration of 12 μM and a temperature of 40 K. To this end, we simulated a water–glycerol glass box with a density expected according to [34,35], estimating the glass transition temperature as T_g = 158 K according to [36]. We used the OPLS-AA force field and a recent parametrisation for glycerol [37] (see Supporting Information Section S2). After testing for convergence, we selected pairs up to an electron–proton distance of 35 Å and a proton–proton distance of 6 Å. We simulated the decay due to the product of 246'230 proton pair ESEEM traces averaged over 221 magnetic field orientations with respect to the atom coordinates. In general, the experimental Hahn echo decay is known to feature a fast contribution stemming from the methyl groups of the nitroxide and a slow contribution from the nuclear spin bath [22,27,29]. In the cases considered here, the methyl tunnel ESEEM component is virtually eliminated by deuteration of the methyl groups. As seen in Fig. 4, the experimental data (grey dots) is rather nicely predicted by the product of nuclear pair ESEEM signals (red curve). The scatter of the experimental data at early times stems from single-nucleus ESEEM. Here and in the following, we have normalised the experimental data by fitting them with a single stretched exponential function and setting the amplitude of this function at $T = 0$ to unity. We prefer this to normalisation with a fit on top of the modulation as used in earlier

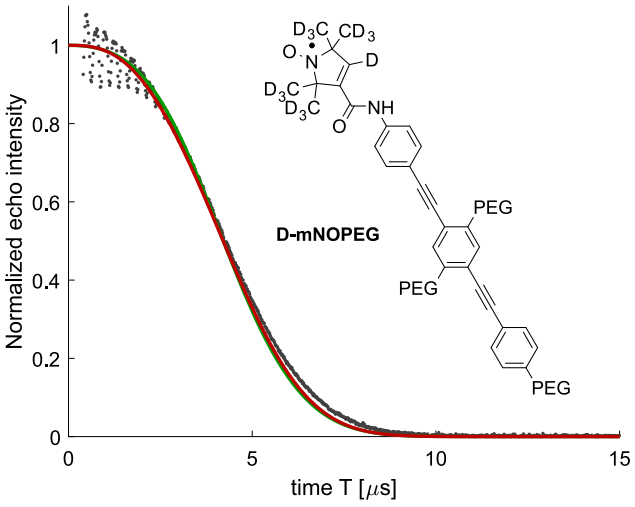

Fig. 4. Hahn echo decay of D-mNOPEG (inset) at a concentration of 12 μM in 1:1 water/glycerol v/v and a temperature of 40 K (dark grey dots) and prediction by the APPA expression (16). The red line is based on the water/glycerol box obtained with the OPLS-AA force field and the green line on the box published as Supporting Information of [30]. (For interpretation of the references to colour in this figure legend, the reader is referred to the web version of this article.)
Source: Experimental data taken from [27].

analysis of this data [27], because destructive interference of single-nucleus ESEEM introduces an additional decay component when fitting on top. The APPA prediction depends only slightly on the model for the water–glycerol glass, as seen by the green curve that nearly coincides with the red curve. The green curve was simulated with the water–glycerol box model published recently by Jahn et al. [30].

The simulation allows us to estimate the electron–proton distance range where proton pairs contribute most strongly to electron spin decoherence. To this end we binned products of nuclear pair ESEEM signals with a resolution of 0.2 Å electron–proton distance. If the two protons of a pair fell into different bins, the square root of the nuclear pair ESEEM signal was assigned to each of the bins. The total decay curve shown in red in Fig. 4 is the product of all bins. Fig. 5(a) demonstrates that the fastest decay is caused by protons at distances between about 6 Å and 10 Å. The contribution of proton pairs at distances to the electron spin shorter than 5 Å can be neglected, whereas proton pairs up to distances of about 25 Å contribute perceptibly. This distance range appears to be somewhat longer than the one found by CCE simulations for a pure water box [25]. However, this is only a consequence of the sensitivity of the visualisation in Fig. 5 to longer times. The visualisation used in [25] is most sensitive near the phase memory time of 4 μs found in this study. As seen in Fig. 5(b), we obtain very similar results as Canarie et al. at this time, whereas proton pairs at longer distances contribute more strongly at longer times when little signal remains (Fig. S1 in the Supporting Information).

4. Dynamical decoupling

Extension of the approach in the previous section to Carr–Purcell sequences with $N = 2\ldots5$ pulses (CP2,CP3, CP4, and CP5 sequences) is straightforward. For $N = 2$ we find

$$W(T) = \frac{1}{64}\left[5\cos(2\eta) + 10\cos(4\eta) - 5\cos(6\eta) + 54\right] + 2\sin^4\eta\cos^2\eta\cos\left(\frac{1}{4}\omega_{\mathrm{nZQ}}T\right) + 2\sin^4\eta\cos^2\eta\cos\left(\frac{1}{2}\omega_{\mathrm{nZQ}}T\right) - 2\sin^4\eta\cos^2\eta\cos\left(\frac{3}{4}\omega_{\mathrm{nZQ}}T\right)$$

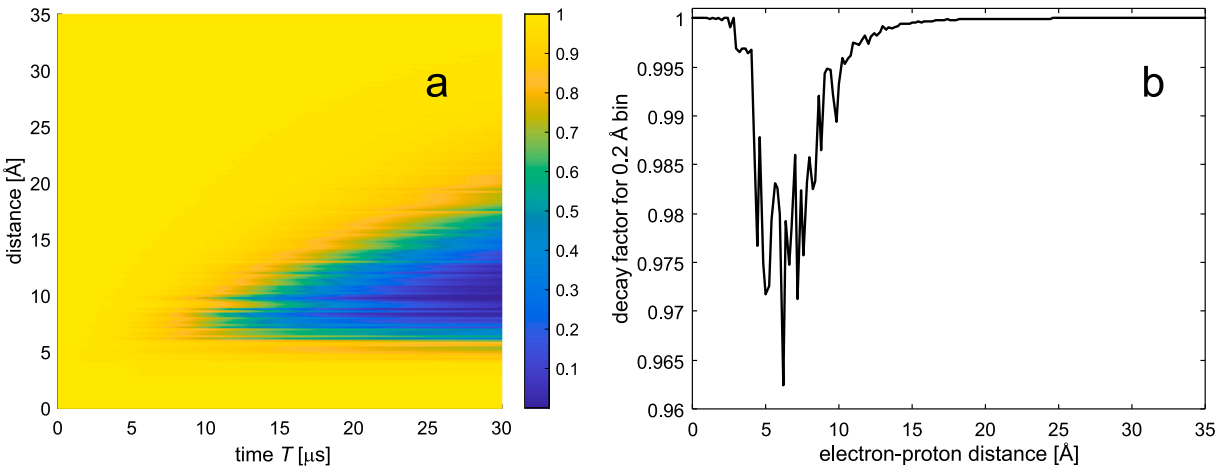

Fig. 5. Dependence of the nuclear pair ESEEM contribution to Hahn echo decay on distance between the electron spin and proton pairs. (a) Shown is the decay factor due to pairs in 0.2 Å wide bins as a function of total sequence length T and distance. (b) Shown is the dependence of the decay factor due to pairs in 0.2 Å wide bins as a function of distance for a total sequence length $T = 4\mu s$.

$$+\frac{1}{2}\sin^4\eta\cos^2\eta\cos\left(\omega_{\mathrm{nZQ}}T\right)\ . \tag{18}$$

This can also be written in a more compact form as

$$W(T) = 1 - 4\sin^4\eta\cos^2\eta\sin^4\left(\frac{\omega_{\mathrm{nZQ}}T}{8}\right) \times \sin^2\left(\frac{\omega_{\mathrm{nZQ}}T}{2}\right)/\cos^2\left(\frac{\omega_{\mathrm{nZQ}}T}{4}\right)\ . \tag{19}$$

The expressions for $N = 3$ (CP3 sequence) and $N = 4$ (CP4 sequence) are given in Section S3 of the Supporting Information. For the CP2 sequence, the leading term in a Taylor expansion for small $\omega_{\mathrm{nZQ}}T$ is of the sixth power in T and ω_{nZQ}. We find for $\omega_{\mathrm{nZQ}}T \ll 1$

$$W(T) \approx 1 - \frac{\sin^4\eta\cos^2\eta}{4096}\left(\omega_{\mathrm{nZQ}}T\right)^6\ . \tag{20}$$

The main contributions to dynamical decoupling are immediately apparent in Eq. (18). Some of the modulation terms have lower frequencies than for the Hahn echo and the amplitude of the modulated terms is reduced. The reduction is apparent from scaling of the modulated terms with $\sin^4\eta$ rather than with $\sin^2\eta$ as in the case of the Hahn echo. The maximum value of $\sin^2\eta = 1$ corresponds to $\cos^2\eta = 0$, where modulation vanishes. For most nuclear spin pairs, $\sin^2\eta \ll 1$, which leads to strong suppression of the modulation, and thus of echo decay. Note that for $N = 3$ refocusing pulses, there exist modulation terms that do not feature an additional factor $\sin^2\eta$ (see Eq. (S3) in the Supporting Information). However, the frequency of these terms is reduced by a factor of three compared to the Hahn echo. For an even number of π pulses, as in the CP2 and CP4 sequences, modulation terms that scale with only $\sin^2\eta$ cancel by symmetry. For each coherence transfer pathway that causes such modulation, there is a symmetric pathway that causes the same modulation with opposite sign of the phase.

Fig. 6a shows that prediction of echo decay by the APPA (red line) is in much worse agreement with experiment (dark grey dots) for the CP2 sequence than it is for the Hahn echo sequence (compare to Fig. 4). Some worsening is expected, as the signal persists to longer times, where perturbation of pair modulation by coupling to further nuclear spins will be more apparent. However, at first sight it is surprising to which extent agreement deteriorates. This deterioration may be explained by the expected scaling of the modulation depth due to correlation of spin pairs p_1 and p_2 with $\sin^2\eta_{p_1}\sin^2\eta_{p_2}$. For the Hahn echo, this scaling factor is much smaller than the one for pairs. For the CP2 sequence, where the scaling factor for pairs is proportional to $\sin^4\eta_p$, correlation contributions are expected to be of the same order of magnitude as pair contributions.

Even more surprisingly, for the CP3 sequence, the APPA predicts faster decay than is experimentally observed (Fig. 6b). For the CP4 sequence, we again find that the decay predicted by the APPA is slower than the one observed experimentally (Fig. 6c), whereas for the CP5 sequence, it is slightly faster (Fig. 6d).

5. Cluster factorisation

The Hahn echo decay can be predicted quite well by the APPA (Fig. 4). The same does not apply to Carr–Purcell echo decays (Fig. 6). This suggests that the Carr–Purcell experiments, in particular the ones with an even number of π pulses, are more sensitive to correlations between pairs. For the dense proton bath we are dealing with, studying this issue by CCE computations of increasing order is computationally very expensive. The matching condition Eq. (14) and scaling of the nuclear pair modulation depth with $\sin^2\eta$ suggest that only a small fraction of pairs interact significantly with each other. However, any attempt to cluster solely by considering $\sin^2\eta$ led us to cluster sizes that were still intractably large.

This raises the question why the pair product approximation works so well for the Hahn echo decay. We find that an interaction can be neglected for a pair (k,l) even if $\sin^2\eta_{kl}$ is sizeable, provided that $\omega_{\mathrm{nZQ},kl}T$ is sufficiently small. In other words, all interactions are negligible that are too small to cause significant phase gain during the time where the echo signal decays below noise level. This effect is somewhat akin to dipolar truncation in solid-state NMR [38]. As a measure of significance of a pair (k,l) of nuclei, we can thus consider $\lambda_{kl}[1-\cos(\omega_{\mathrm{nZQ},kl}t)]$ at times t shorter than the typical decay time. In particular, we are interested in a threshold, where the pair (k,l) does not significantly perturb spin dynamics in a cluster that contains nucleus k, but not nucleus l. The perturbation is negligible either if λ_{kl} is very small or if $\omega_{\mathrm{nZQ},kl}t \ll 1$. In both cases, we can approximate $\cos(\omega_{\mathrm{nZQ},kl}t)$ by $\cos x \approx 1 - x^2/2$. Hence, in clustering we can neglect interactions with $\theta_{kl} < \epsilon$, where

$$\theta_{kl} = \frac{\lambda_{kl}}{2}\omega_{\mathrm{nZQ},kl}^2 \tag{21}$$

and ϵ is a suitably low threshold. We estimated ϵ as follows. In the prediction of Hahn echo decay we neglected pairs with $\theta_{kl} < \epsilon$ and increased ϵ until the prediction deviated from the prediction for $\epsilon = 0$ by more than 1% of the echo maximum. We found that a threshold $\epsilon = 1\cdot 10^{-5}$ $(\mathrm{Mrad/s})^2$ provides good predictions. Here and in the following, Mrad/s denotes an angular velocity of 10^6 radian per second.

With this in mind, we perform clustering based on a list of all pairs (k,l) with $\theta_{kl} > \epsilon$, starting from the pair with maximal θ_{kl}. The nucleus with index n, for which the sum $\theta_{kn}+\theta_{ln}$ is maximal is added to provide a cluster of size 3. The procedure is iterated up to a maximum cluster

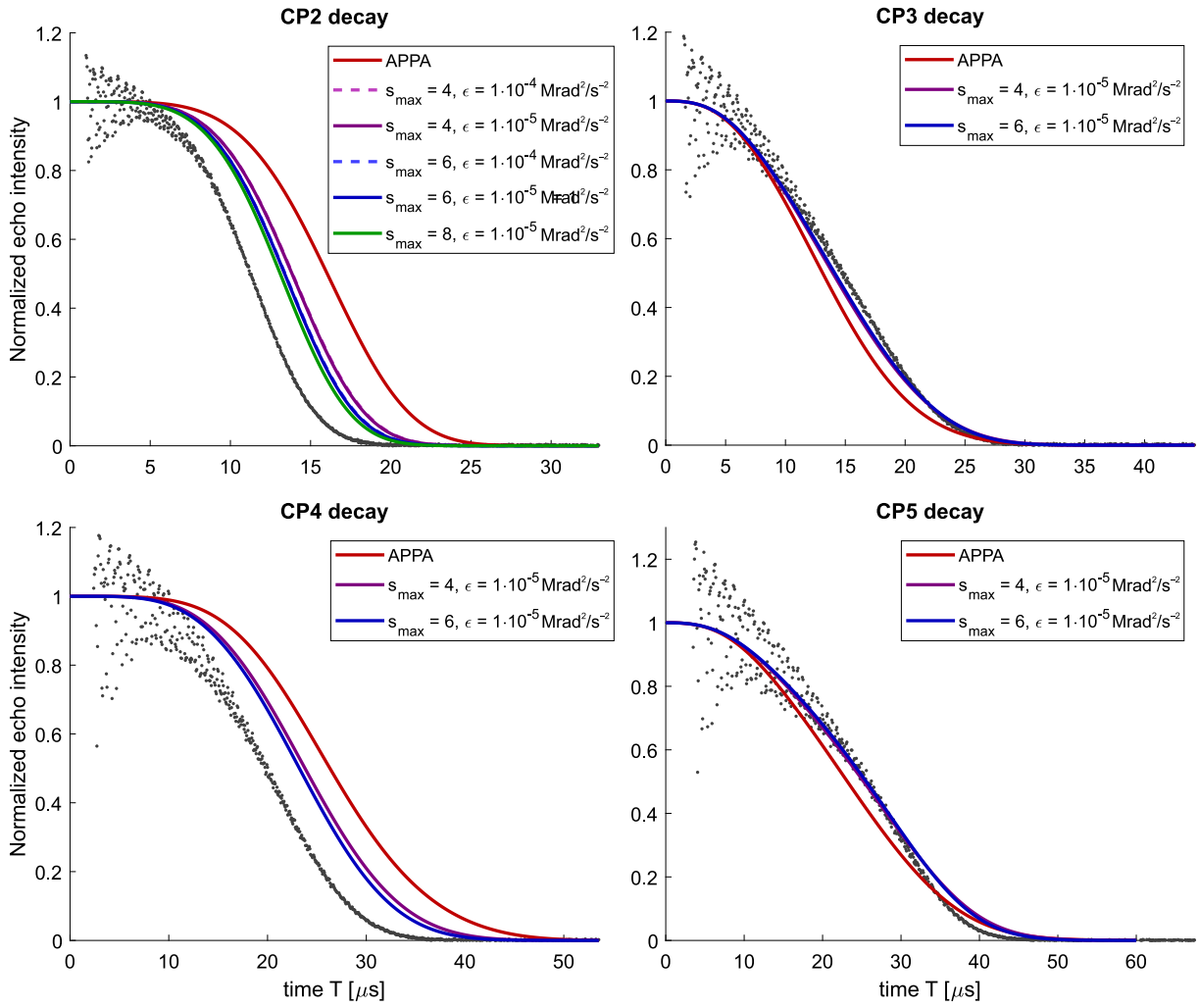

Fig. 6. Prediction of Carr–Purcell echo decays in 1:1 water/glycerol v/v by different approaches and comparison with experiments performed on D-mNOPEG at a concentration of 12 μM and a temperature of 40 K (dark grey dots). Amplitude of the experimental data was normalised by fitting a stretched exponential decay. Experimental data taken from [27]. Red lines correspond to the APPA predictions and all lines with other colours to cluster factorisation with parameters indicated in the legend. (For interpretation of the references to colour in this figure legend, the reader is referred to the web version of this article.)

size $s_{\max}$ by always adding the nucleus with index n that maximises $\sum_i \theta_{in}$, where index i run over all nuclei already belonging to the cluster. At this point, the cluster is stored and all pairs of nuclei within this cluster are removed from further consideration. The procedure is then repeated with the pair from the remaining list that features maximal θ_{kl}. In practice, we found that most nuclei were assigned to clusters with the maximum size $s_{\max}$. This still leaves a large list of remaining pairs (n, m) of nuclear spins that belong to different clusters but have $\theta_{nm} > \epsilon$. Modulation due to these pairs must be considered as well. At $\epsilon = 1 \cdot 10^{-5}$ $(\mathrm{Mrad/s})^2$ we obtained about 1090 clusters and about 21 800 pairs from a water–glycerol sphere with radius 25 Å at $s_{\max} = 4$. These numbers depend slightly on orientation of the water–glycerol box with respect to magnetic field.

Computational effort increases drastically with increasing $s_{\max}$, since Hilbert size dimension scales with $2^{s_{\max}}$ and computation time for matrix multiplications scales with the third power of Hilbert size dimension. Simulations of echo decays are feasible for $s_{\max} \leq 8$. An alternative approach for considering more correlations lies in reducing the threshold ϵ. To this end we considered all 9156 protons in the 50×50×50 Å^3 water–glycerol box. At $s_{\max} = 4$ and $\epsilon = 1 \cdot 10^{-6}$ $(\mathrm{Mrad/s})^2$ we obtained about 2200 clusters and 176 000 pairs.

Considering cluster correlations in this way does not significantly alter the predictions for Hahn echo decay (Supplementary Fig. S2). In contrast, predictions for Carr–Purcell echo decays differ substantially from the ones obtained by the APPA. For the CP2 sequence we performed computations with $s_{\max} = 4, 6$ and 8 at $\epsilon = 1 \cdot 10^{-5}$ $(\mathrm{Mrad/s})^2$ and with $s_{\max} = 4$ and 6 at $\epsilon = 1 \cdot 10^{-4}$. The results are shown in Fig. 6. Decreasing ϵ from $1 \cdot 10^{-4}$ $(\mathrm{Mrad/s})^2$ to $1 \cdot 10^{-5}$ $(\mathrm{Mrad/s})^2$ has almost no effect. Therefore, we refrained from computations with $\epsilon = 1 \cdot 10^{-6}$ $(\mathrm{Mrad/s})^2$. In contrast, increasing $s_{\max}$ from 4 to 6 improves the simulation substantially. Further minor improvement is observed by increasing $s_{\max}$ to 8. At this point, cluster factorisation appears to be converged. The converged prediction is significantly better than the prediction obtained by the APPA. Yet, it still differs substantially from the experimental result.

For the remaining Carr–Purcell sequences we performed computations with $s_{\max} = 4$ and 6 at $\epsilon = 1 \cdot 10^{-5}$ $(\mathrm{Mrad/s})^2$. For odd numbers of π pulses (CP3, CP5), cluster factorisation appears to be nearly converged already at $s_{\max} = 4$. Interestingly, for these cases cluster factorisation indeed predicts slower decay than application of the APPA. Although the simulations for the CP3 and CP5 sequences are not as good as for the Hahn echo sequence, they rather nicely predict the sequence duration $T_{1/2}$ where the echo decays to half its maximum amplitude. In contrast, for the CP4 sequence discrepancy between the simulated and experimental decay is similar to the one for the CP2 case.

We checked whether this discrepancy is caused by the model of the water–glycerol glass obtained by molecular dynamics simulations (Fig. 7). For this, we compared the simulated CP2 decay for two

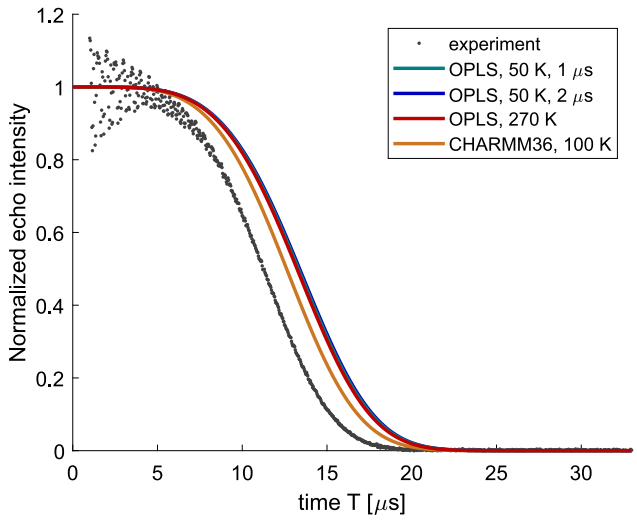

Fig. 7. Comparison of predictions of the CP2 echo decay by cluster factorisation with different models for the water–glycerol glass. The grey dots are experimental data taken from [27] and the coloured lines correspond to different glass models as described in the legend and main text. (For interpretation of the references to colour in this figure legend, the reader is referred to the web version of this article.)

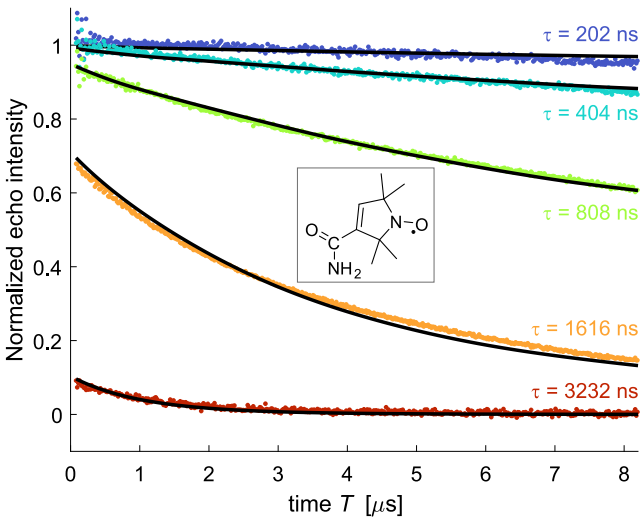

Fig. 8. Experimental stimulated echo decays (coloured dots) for 25 μM 3-amido-Proxyl (inset) in 1:1 water/glycerol v/v at a temperature of 50 K at different first interpulse delays τ as indicated on the right. The black lines correspond to simulations by the analytical expression Eq. (22) using a water/glycerol 1:1 (v/v) glass box described in Section S2 of the Supporting Information. Vertical scaling was fitted separately for each value of τ. (For interpretation of the references to colour in this figure legend, the reader is referred to the web version of this article.)

trajectory frames at 1 μs (green line) and 2 μs (blue line) from our MD simulation at 50 K, for the final frame of our MD simulation at 270 K (red line), and for the water–glycerol box published by Jahn et al. [30]. While our glass models were obtained with the OPLS-AA force field (OPLS-DES parametrisation for glycerol [37], simple point charge model for water), the water–glycerol box from [30] is based on the CHARMM36 force field. The difference between the two OPLS-AA trajectory frames at 50 K is minor. Likewise, the difference between OPLS-AA simulations at 50 K and 270 K is small. Note that we used the density estimate for a temperature of 50 K also in the simulation at 270 K. In contrast, the difference between our OPLS-AA simulations and the CHARMM36 simulation from [30] is sizeable. This result does not depend on whether we include all protons in the respective boxes or only protons in a sphere with radius 25 Å. All these simulations substantially underestimate experimental CP2 echo decay. The result suggests that the CHARMM36 force field provides a better model for the water–glycerol glass than the OPLS-AA force field. However, given the remaining deviation from experiment and its unknown origin, we cannot safely conclude this. We tentatively assign the remaining deviation to the use of ideal (infinitely short) pulses in our simulation, which was necessitated by an accuracy of the numerical matrix exponential that is too poor for performing simulations with pulses of finite length.

As seen in Fig. S3 in the Supporting Information, differences between glass models are almost negligible in cluster factorisation simulations of the Hahn echo decay and very minor for the CP3 and CP5 experiments with odd numbers of π pulses. For the CP4 experiment, the difference is pronounced, yet smaller than for the CP2 experiment. This suggests that the CP2 echo decay is most sensitive to local glass structure. That the Hahn echo decay is rather insensitive to the glass model can be explained by its insensitivity to correlations between more than two protons. Presumably, Hahn echo decay is dominated by proton pairs bound to the same heavy atom. Bond lengths and bond angles are expected to agree closely between different force fields. The correlations detected by the CP2 experiment are likely to involve protons that are connected by hydrogen bonds. Hydrogen-bond geometry is expected to vary more strongly between different force fields.

6. Stimulated echo decay

In analogy to single-nucleus ESEEM, we expected that echo modulation should also arise for a stimulated echo sequence $(\pi/2)-\tau-(\pi/2)-T-(\pi/2)-\tau-echo$. We computed the corresponding analytical expression by assuming suppression of other echoes by phase cycling. Since the result depends on electron spin resonance offset Ω_S, we integrated it over an infinitely broad uniform distribution of Ω_S. We computed the expressions W^α for the electron spin in the α state and W^β for the electron spin in the β state during delay T separately. As known from the case of single-nucleus ESEEM, in principle, the expressions for W^α and W^β need to be multiplied separately [32]. Because of the symmetry of the nuclear-pair ESEEM problem, we find $W^\alpha = W^\beta = W$ with

$$W(T,\tau) = 1 - 2\lambda \sin^2\left(\frac{\omega_{\mathrm{nZQ}}}{2}\tau\right) \times \left[1 - \cos\left(\omega_{\mathrm{nZQ}}(\tau+T)\right)\right] \quad (22)$$

Hence, in the APPA for nuclear-pair ESEEM, we can multiply the W instead of separately multiplying the W^α and W^β. The symmetry arises from evolution of nuclear zero-quantum coherence during time T. The frequency ω_{nZQ} of this coherence does not depend on electron spin state.

The expression (22) reveals why decay of the stimulated echo is much slower than decay of the Hahn echo, despite the fact that modulation depth is the same and that the modulation frequency with respect to time T is of the same order of magnitude. The equivalent of the three-pulse ESEEM blindspot factors

$$\sin^2\left(\frac{\omega_{\mathrm{nZQ}}}{2}\tau\right) = \frac{1}{2}\left[1 - \cos\left(\omega_{\mathrm{nZQ}}\tau\right)\right] , \quad (23)$$

is small at typical values of the first interpulse delay τ, causing attenuation of the decay compared to the Hahn echo decay. The increase of this factor with increasing delay τ explains why the stimulated echo decays the faster the longer τ is.

Fig. 8 compares predictions based on Eq. (22) and the APPA with experimental data obtained on 3-amido-Proxyl in a 1:1 (v/v) water–glycerol glass at 50 K at different delays τ (coloured dots). We have

confirmed by an inversion recovery experiment that longitudinal relaxation is much slower than stimulated echo decay under these conditions (Fig. S4 in the Supporting Information). The initial amplitude at $T = 0.08$ µs is strongly affected by conventional single-nucleus ESEEM, whose prediction would require knowledge of the proton hyperfine couplings of the spin probe. Therefore, we scaled amplitude of the experimental decay traces individually for each value of τ. With this provision, the APPA predicts stimulated echo decay quite well. Residuals are shown in Fig. S5 in the Supporting Information.

7. Relation to spectral diffusion models

Faster decay of the stimulated echo than by the longitudinal relaxation rate $1/T_1$ and the dependence of this decay on interpulse delay τ have been previously explained by a different picture. In this picture, the subsequence $(\pi/2) - \tau - (\pi/2)$ generates a polarisation grating $\cos(\Omega_S\tau)$ [32]. The stimulated echo is, effectively, the free induction decay of this grating. Spectral diffusion levels the polarisation grating, thus leading to stimulated echo decay. As a longer interpulse delay τ causes a finer grating on the frequency scale, the rate of levelling increases with increasing τ. At low temperature and high dilution, the underlying spectral diffusion was assumed to stem from nuclear spin flip-flops, which change the electron spin resonance frequency by the difference of the hyperfine couplings to the two nuclei.

The microscopic mechanism for stimulated echo decay suggested by the nuclear pair ESEEM treatment is different. The longer τ is, the more electron spin magnetisation is transferred to nuclear pair zero-quantum coherence. This coherence decays during time T due to the large number of nuclear spin pairs with non-negligible modulation depth and the distribution of their zero-quantum frequencies ω_{nZQ}. The stochastic aspect arises from random distribution of protons around each individual electron spin. A phenomenological description in terms of a diffusion equation can still be appropriate. In fact, in recent work signal decay for the related constant-time five-pulse RIDME sequence as a function of two parameters related to delays τ and T could be globally fitted with a two-parameter nuclear spin diffusion model [21]. Further work will be required for understanding the relation between the two approaches in a quantitative manner.

8. Relation to spectral density of spin noise

Previous analysis of a series of a set of multi-pulse echo decay data in terms of a nuclear spin noise spectrum provided consistent results for Carr–Purcell and Uhrig dynamical decoupling sequences with $N = 2 \ldots 5$ pulses [29]. Here we construct the noise spectrum S from first principles, using Eq. (12) and our spatial model of the nuclear spin bath (water–glycerol glass). We assume that the APPA holds and that each nuclear pair contributes only a very small fraction to Hahn echo decay. First, we note a similarity between Eq. (12) and the filter function $F(z) = F(\omega T)$ given for the Hahn echo in [14],

$$F(z) = 8\sin^4\left(\frac{z}{4}\right) = 8\sin^4\left(\frac{\omega T}{4}\right) . \tag{24}$$

By substituting $\omega = \omega_{\mathrm{nZQ}}$, we can formally rewrite the APPA expression for Hahn echo decay, Eq. (16), as

$$W(T) = \prod_p \left[1 - \frac{\lambda_p}{2} F(\omega_{\mathrm{nZQ},p} T)\right] . \tag{25}$$

The quantity that can be predicted from the filter function F and the noise spectrum S is the attenuation function $\chi(T) = -\ln W(T) = \int_0^\infty \mathrm{d}\omega/\pi\ FS/\omega^2$ [18]. We have

$$\begin{aligned}\chi(T) &= -\sum_p \ln\left(1 - \frac{\lambda_p}{2} F(\omega_{\mathrm{nZQ},p} T)\right) \\ &\approx \sum_p \frac{\lambda_p}{2} F(\omega_{\mathrm{nZQ},p} T) ,\end{aligned} \tag{26}$$

where we have substituted $\ln(1 - x) \approx -x$, which is justified by $\lambda_p F(\omega_{\mathrm{nZQ},p} T)/2 \ll 1$ for any individual pair at times T where the Hahn echo is still observable.

Using $\chi(T) = \int_0^\infty \mathrm{d}\omega/\pi\ FS\omega^2$, Eq. (26) can be interpreted in terms of individual contributions of nuclear spin pairs with index p to the noise spectrum. Each pair contributes spectral density

$$S_{\mathrm{Hahn},p} = \frac{\pi}{2}\cos^2\eta_p \sin^2\eta_p \omega^2_{\mathrm{nZQ},p}\delta(\omega - \omega_{\mathrm{nZQ},p}) , \tag{27}$$

where δ denotes the Dirac δ function. With a noise spectrum computed in this way and the analytical filter function for the Hahn echo, we can indeed reproduce the Hahn echo decay (red line in panel 'Hahn echo' of Fig. 9). We note that, up to a constant factor, the spin-noise contribution (27) of a homonuclear pair, matches our factorisation criterion θ_{kl}(21). The same noise spectrum does not, however, predict the effect of dynamical decoupling very well (red lines in panels CP2). This is not entirely unexpected. In previous work, the noise spectrum that provided a consistent description for Carr–Purcell and Uhrig dynamical decoupling sequences with $N = 2 \ldots 5$ pulses led to rather poor agreement for Hahn echo decay [29].

In fact, inconsistency of noise spectrum formalism between the Hahn echo and the CP2 echo within the APPA can be proved. The pair contribution to the noise spectrum for the CP2 sequence can be derived in an analogous way as for the Hahn echo sequence, since the modulation expression in Eq. (19) agrees with the filter function for the CP2 sequence. We find that each pair contributes spectral density

$$S_{\mathrm{CP2},p} = \frac{\pi}{2}\cos^2\eta_p \sin^4\eta_p \omega^2_{\mathrm{nZQ},p}\delta(\omega - \omega_{\mathrm{nZQ},p}) . \tag{28}$$

This contribution contains an additional factor $\sin^2\eta_p$ with respect to the Hahn echo case. This factor is smaller than unity and thus reduces noise spectral density as compared to the Hahn echo case. We have ascertained that the noise spectrum for the CP2 sequence derived in this way reproduces the CP2 echo decay as predicted by applying the APPA.

We tested whether inconsistency of the description of Hahn and CP2 echo decay in terms of a noise spectrum is entirely due to deficiencies of the APPA. To this end, we established a parametric model for the noise spectrum. We found that the noise spectrum computed with the analytical expression for the water–glycerol box model is well approximated by a sum of two stretched exponential terms,

$$\begin{aligned}S(\omega) \approx\ & A_1 \exp\left[-\left(\frac{\omega}{\omega_1}\right)^{\xi_1}\right] \\ & + A_2 \exp\left[-\left(\frac{\omega}{\omega_2}\right)^{\xi_2}\right] .\end{aligned} \tag{29}$$

Each individual Carr–Purcell echo decay can be fitted well by assuming a noise spectrum of this form (see ochre lines in panels CP2-CP5 of Fig. 9). However, a global fit to all Carr–Purcell decays (blue lines) provides a very good approximation only for the two cases with an even number of π pulses (CP2 and CP4). For the CP3 and CP5 cases, agreement is only fair. This suggests that prediction of dynamical decoupling by a noise spectrum provides a good approximation only if the number of π pulses is sufficiently large or if it is even. Prediction of Hahn echo decay via expression (27) is of interest because of its computational efficiency, which is substantially better even than the one of the APPA.

9. Refocusing of nuclear pair ESEEM

In recent work with the refocused echo sequence $(\pi/2) - \tau_1 - (\pi) - \tau_1 - \tau_2 - (\pi) - \tau_2 - echo$, an increase of the echo amplitude was observed upon increasing τ_1 at a fixed long τ_2 [28]. This suggests that electron spin coherence decay due to nuclear pair ESEEM can be partially reversed. In other words, the second π pulse refocuses part of the nuclear zero-quantum echo modulation.

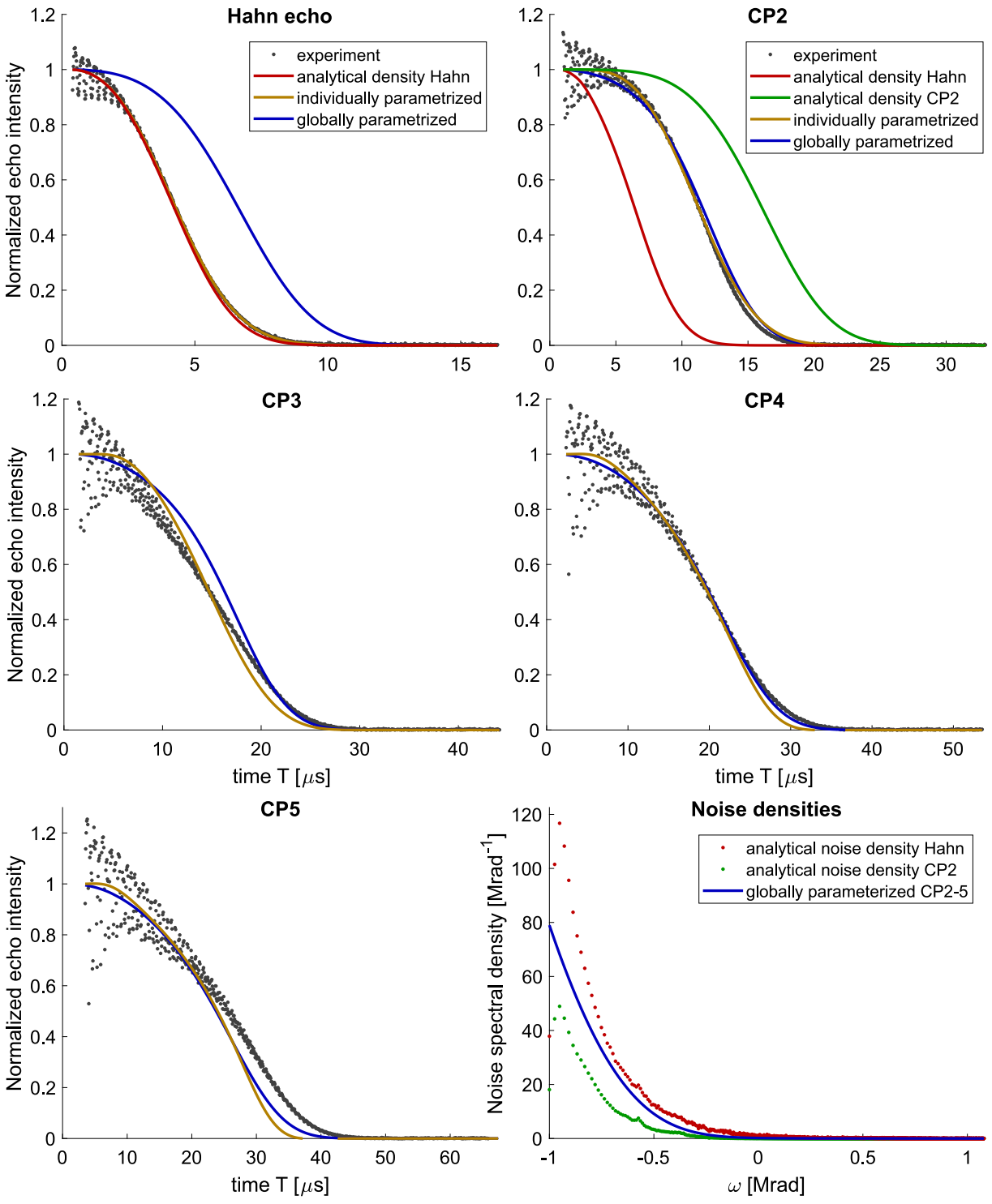

Fig. 9. Prediction of echo decays in 1:1 water/glycerol v/v via noise spectra and comparison with experiments performed on D-mNOPEG at a concentration of 12 μM and a temperature of 40 K (dark grey dots). Amplitude of the experimental data was normalised by fitting a stretched exponential decay. Experimental data taken from [27]. The red lines correspond to the analytical expression (27) for noise density governing Hahn echo decay, the green line to the analytical expression (28) for the CP2 experiment, the ochre lines were obtained by fitting the empirical expression (29) for the noise spectrum to individual echo decays and the blue line by fitting it globally to the Carr–Purcell echo decays with $2\cdots5$ π pulses. (For interpretation of the references to colour in this figure legend, the reader is referred to the web version of this article.)

In order to obtain insight into this phenomenon, we have derived the nuclear pair ESEEM expression for this experiment,

$$\begin{aligned} V(\tau_1,\tau_2) = {} & \frac{1}{64}\left[3\cos(2\eta)+14\cos(4\eta)\right. \\ & \left.-3\cos(6\eta)+50\right] \\ & +\sin^2\eta\cos^4\eta\cos\left[\omega_{\mathrm{nZQ}}\left(\tau_1-\tau_2\right)\right] \\ & -\frac{1}{2}\sin^2\eta\cos^4\eta\cos\left(2\omega_{\mathrm{nZQ}}\tau_1\right) \\ & -\frac{1}{2}\sin^2\eta\cos^4\eta\cos\left(2\omega_{\mathrm{nZQ}}\tau_2\right) \\ & -\sin^2\eta\cos^2\eta\cos\left[\omega_{\mathrm{nZQ}}\left(\tau_1+\tau_2\right)\right] \\ & -\sin^4\eta\cos^2\eta\cos\left[\omega_{\mathrm{nZQ}}\left(\tau_1+\tau_2\right)\right] \end{aligned}$$

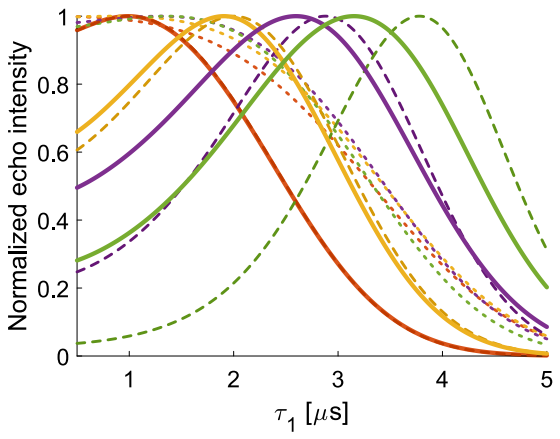

Fig. 10. Predictions of refocused echo decay with respect to the first interpulse delay τ_1 at fixed interpulse delays $\tau_2 = 1$ µs (red), 2 µs (yellow), 3 µs (violet) and 4 µs (green). The predictions can be compared to experimental results (Fig. 3(c) in [28]), which are closest to the thick solid lines, but with maxima occurring at still earlier times. Dotted lines are predictions from the noise spectrum fitted to CP2-5 decays, dashed lines (slightly darker hue) are predictions from the analytical expression Eq. (30), and thick solid lines are predictions by cluster factorisation. All traces are amplitude-normalised to their respective maxima. Traces normalised to Hahn echo amplitude are shown in Fig. S6 in the Supporting Information. (For interpretation of the references to colour in this figure legend, the reader is referred to the web version of this article.)

$$
\begin{aligned}
&+ \sin^4\eta\cos^2\eta\cos\left(\omega_{\mathrm{nZQ}}\tau_1\right)\\
&+ \sin^4\eta\cos^2\eta\cos\left(\omega_{\mathrm{nZQ}}\tau_2\right)\\
&+ \frac{1}{2}\sin^4\eta\cos^2\eta\cos\left[2\omega_{\mathrm{nZQ}}\left(\tau_1+\tau_2\right)\right]\\
&- \sin^4\eta\cos^2\eta\cos\left[\omega_{\mathrm{nZQ}}\left(2\tau_1+\tau_2\right)\right]\\
&- \sin^4\eta\cos^2\eta\cos\left[\omega_{\mathrm{nZQ}}\left(\tau_1+2\tau_2\right)\right]
\end{aligned}
\tag{30}
$$

Since $\sin\eta \ll 1$ for most proton pairs, terms with factors $\sin^4\eta$ typically contribute much less to modulation than terms with factors $\sin^2\eta$. The second term on the right-hand side with time dependence $\cos\left[\omega_{\mathrm{nZQ}}\left(\tau_1-\tau_2\right)\right]$ leads to a nuclear zero-quantum echo at $\tau_1 = \tau_2$.

Predictions by Eq. (30) can be compared to experimental results shown in Fig. 3(c) of [28]. To this end, we have computed traces in the range $\tau_1 = 0\cdots5$ µs for values of $\tau_2 = 1, 2, 3$, and 4 µs and plotted them as dashed lines in Fig. 10 in the same range and with the same normalisation as in [28]. Qualitatively, the increase of echo amplitude with increasing length of the pulse sequence is reproduced. However, the effect predicted by the APPA is more dramatic than the one observed experimentally. Further, in the APPA the maxima occur almost exactly at $\tau_1 = \tau_2$, whereas they occur at earlier times in the experimental observation. Both discrepancies are alleviated, but not completely removed, by predicting the behaviour with cluster factorisation (solid lines in Fig. 10). In both cases, the predicted maxima have a smooth, round shape, whereas for $\tau_2 = 1$ and 2 µs they feature cusps in the experimental data in [28]. As suggested by Andrea Eggeling, we tentatively assign these cusps to methyl tunnel ESEEM [29]. For the shortest delay $\tau_2 = 1$ µs, predictions by the analytical expression and by cluster factorisation almost coincide.

We have also tested prediction for the refocused echo sequence based on the noise spectrum. For this, we used the noise spectrum fitted to the CP2, CP3, CP4, and CP5 decay, which predicts CP2 decay quite nicely as seen in Fig. 9. The CP2 and refocused echo sequences differ only in the choice of interpulse delays and in delay incrementation. Yet, prediction via the noise spectrum fails even qualitatively for the refocused-echo case (dotted lines in Fig. 10). This is not unexpected, as a stochastic approach cannot account for the coherent refocusing to a nuclear zero-quantum echo.

Fig. S6 in the Supporting Information shows predicted decays that are normalised to the maximum Hahn echo amplitude. As expected, they reveal that the APPA overestimates the extent of refocusing compared to the prediction by cluster factorisation. Quantitative understanding of the dependence of echo amplitude on the interpulse delays τ_1 and τ_2 of the refocused echo sequence will require further work and may depend on simulations with finite pulse length as well as on considering the methyl tunnel ESEEM contribution.

10. Conclusion

Homonuclear spin pairs in the vicinity of an electron spin give rise to echo modulation if the difference of the two hyperfine couplings is similar to the dipole–dipole coupling between the nuclear spins. In the absence of methyl groups and at sufficiently low temperatures and sufficiently low electron spin concentration, the combination of such nuclear pair echo modulations with different frequencies dominates electron spin echo decay. Analytical expressions for the modulation due to a single pair of nuclei can be obtained by product operator formalism and provide qualitative insight into the time dependence of echo amplitude for the Hahn echo, the refocused echo, the stimulated echo and for echoes after Carr–Purcell sequences with a small number of refocusing pulses. Hahn echo decay of a nitroxide radical in water–glycerol glass could be predicted rather nicely from a molecular dynamics model of the matrix by approximating it as the product of nuclear pair ESEEM traces. The same approximation reproduces the dependence of stimulated echo decay upon increasing the second interpulse delay T on the first interpulse delay τ reasonably well. It performs worse for the refocused echo sequence and for Carr–Purcell pulse trains, especially if the number of π pulses is even.

The deficiencies of the APPA arise from the influence of other nuclear spins on the pair modulation, i.e., from correlations between pairs. Because Carr–Purcell sequences with an even number of π pulses refocus all modulation terms that are linear in the transition probability of forbidden transitions, such correlations affect Carr–Purcell echoes after an even number of π pulses more strongly. The correlations can be accounted for by computing a product over disjoint clusters rather than over only pairs. Such cluster factorisation provides good predictions for Carr–Purcell sequences with an odd number of π pulses, but fails to converge to the experimentally observed echo decay for an even number. This failure may be caused by approximating the π pulses as infinitely short pulses in order to avoid problems due to insufficient accuracy of the numerical matrix exponentials.

The expressions for the modulated part of the Hahn and CP2 echo formally coincide with the respective filter functions in the formalism of noise spectroscopy. This allows for deriving spin-noise spectral density for these two sequences within the APPA. These spectral densities differ between the two sequences. Hahn echo decay can be predicted with the best computational efficiency by first computing noise spectral density from the spatial distribution of nuclear pairs and then applying the filter kernel. However, the spin-noise formalism fails to reproduce the dependence of refocused echo amplitude on the two interpulse delays. This failure is caused by the coherent nature of nuclear pair ESEEM, which can lead to echo formation.

Our formalism allows for fast and almost quantitative prediction of Hahn echo decay from a model for the spatial distribution of homonuclear pairs in the vicinity of the electron spin. This opens up a new way for elucidating such a spatial distribution. However, there exist two caveats. First, most systems of interest feature methyl groups in the vicinity of the electron spin. Hence, the problem of methyl tunnel ESEEM [29,39,40] needs to be solved on a similar level. Second, it needs to be established how sensitive such an approach is and whether predictions work as well for other systems as for the water–glycerol glass.

While the microscopic mechanism of electron spin decoherence in the absence of microwave irradiation appears to be well understood now, the same does not necessarily apply to rotating-frame

relaxation [41]. We will check in the near future whether hyperfine-decoupled nuclear pair ESEEM significantly contributes to this type of relaxation.

11. Materials & methods

11.1. EPR measurements

Stimulated echo decays were measured in X-band (≈ 9.75 GHz) at a Bruker Elexsys II E580 spectrometer with a Bruker Flexline probehead EN 4118X-MD-4. Resonator and sample were cooled to a temperature of 50 K using an Oxford flow cryostat and an Oxford ITC 5035 temperature controller. A solution of 25 μM 3-amido-Proxyl (see inset in Fig. 8) in 1:1 water/glycerol v/v was shock-frozen by immersion into liquid nitrogen immediately before the measurements and inserted into the pre-cooled resonator. After recording a field-swept echo detected EPR spectrum, all further experiments were performed at the maximum of the nitroxide spectrum. A shot repetition time of 8 ms was used for stimulated echo decay measurements with sequence $(\pi/2)-\tau-(\pi/2)-T-(\pi/2)-\tau-echo$ and a shot repetition time of 16 ms for inversion recovery measurements with the sequence $(\pi)-T-(\pi/2)-\tau-(\pi)-\tau-echo$. We used a standard 4-step phase cycle for the stimulated echo decay and a $[(+x)-(-x)]$ phase cycle on the $\pi/2$ pulse for inversion recovery. The $\pi/2$ pulse length for stimulated echo decay was 12 ns, with an initial delay $T_0 = 80$ ns and acquisition of 512 data points per τ value with a time increment $\Delta T = 16$ ns. The initial value of the first interpulse delay τ was 202 ns. The measurement of decay at five τ values was implemented as a 2D experiment in PulseSpel, in which both τ and the number of scans was doubled at each step in the second dimension. Data was acquired over a 16 ns integration gate centred at the echo maximum. Inversion recovery was performed with a 24 ns π pulse for inversion and a 24 ns $\pi/2$ and 48 ns π pulse for the observer echo, which had an interpulse delay of 248 ns. For inversion recovery, 512 data points with an increment of $\Delta T_0 = 5$ μs were acquired starting at an initial recovery delay $T_0 = 400$ ns. Data for the Hahn echo decay and Carr–Purcell echo decays of 12 μM D-mNOPEG (see inset in Fig. 4) were taken from [27].

11.2. Modelling of water–glycerol glass

A water–glycerol box with dimension of $50\times50\times50$ Å^3 was generated in GROMACS 2021.2 [42] as follows. Simple point charge water (spc216.gro) was used for the water parameters. The parameters and topology file for glycerol [37] were downloaded from GitHub (https://github.com/orlandoacevedo/DES, accessed 7 October 2022). We estimated the glass transition temperature of a 1:1 (v/v) mixture of water and glycerol as 158 K based on an expression in [36]. We computed the density at the glass transition temperature from data given in [34]. The thermal expansion coefficient of pure glycerol is by about a factor of 5 smaller in the glassy state than in the supercooled liquid [35]. We conjectured that the same factor applies to the water–glycerol mixture and arrived at a density of 1.247 kg/m^{-3} of the glass at 50 K, corresponding to 2306 water molecules and 568 glycerol molecules in the box. We used the same box for comparison to measurements at 40 and 50 K, as the estimate at 40 K (2308 water molecules, and 569 glycerol molecules) does not differ significantly compared to uncertainty of this procedure. The box was annealed by NVT molecular dynamics (MD) simulations starting at 300 K and decrementing temperature in steps of 10 K. At each temperature, a 100 ns trajectory was run. At the final temperature of 50 K we computed at 2 μs long trajectory. This procedure corresponds to much faster cooling than can be achieved experimentally. Nevertheless, we assume that deviations between computation and experiment are dominated by the approximations made in the spin dynamics simulations rather than by approximations in our solvent model. This assumption is supported by the close agreement of Hahn echo simulations with our own solvent box and with the box generated by the Stoll group [30] (see Fig. 7). In ESEEM simulations, 1.15% of the protons were randomly omitted in order to account for natural abundance of deuterium.

11.3. Product operator computations

All computations by product operator formalism were performed in Mathematica (Wolfram Research, Long Hanborough, UK) using a Wolfram language package for this purpose supplied by Serge Boentges.

11.4. Numerical computations

Numerical computations based on analytical expressions and on density operator formalism were performed with home-written Matlab (The MathWorks, Inc., Natick, Ma, USA) scripts. The EasySpin package (Development version 6.0.0-dev34) [43] was used for computation of orientation grids and of matrix representations of spin operators as well as for values of fundamental constants. A spherical orientation grid with C_i symmetry and 7 knots (85 orientations) was used throughout after establishing that prediction of Hahn echo decay by the analytical expression and the product pair approximation did not change significantly when using a larger grid with 313 orientations. Noise spectroscopy simulations reused some code provided by Janne Soetbeer [27].

Declaration of competing interest

The authors declare that they have no known competing financial interests or personal relationships that could have appeared to influence the work reported in this paper.

Data availability

Experimental raw data for stimulated echo decay and inversion recovery, normalised experimental data for Hahn echo decay and Carr–Purcell echo decays from Soetbeer et al., (2021), a Cartesian coordinate file of the water–glycerol box, and Matlab scripts used in numerical computations are available under doi: 10.5281/zenodo.7383253.

Acknowledgements

I gratefully acknowledge helpful discussions with A. Eggeling, L. Fábregas Ibáñez, H. Karas, D. Klose, S. Kuzin, J. Soetbeer, A. Vanas, and M. Yulikov, sample preparation by H. Karas, and software contributions from S. Boentges and J. Soetbeer. I thank an anonymous reviewer for pointing out that frequency shifts induced by the pseudo-secular contribution of the hyperfine coupling can have a substantial effect for certain nuclear spin pairs.

Appendix A. Supplementary data

Supplementary material related to this article can be found online at https://doi.org/10.1016/j.jmro.2023.100094.

References

[1] W.B. Mims, in: S. Geschwind (Ed.), Electron Paramagnetic Resonance, Plenum, New York, 1972, pp. 263–351.
[2] I.A. Brown, in: L. Kevan, R.N. Schwartz (Eds.), Time Domain Electron Spin Resonance, John Wiley & Sons, New York, 1979, pp. 195–229.
[3] A. Zecevic, G.R. Eaton, S.S. Eaton, M. Lindgren, Dephasing of electron spin echoes for nitroxyl radicals in glassy solvents by non-methyl and methyl protons, Mol. Phys. 95 (6) (1998) 1255–1263, http://dx.doi.org/10.1080/00268979809483256, URL http://www.tandfonline.com/doi/abs/10.1080/00268979809483256.
[4] G.R. Eaton, S.S. Eaton, Distance measurements in biological systems by EPR, in: L.J. Berliner (Ed.), Biological Magnetic Resonance, Vol. 19, Kluwer Academic/Plenum Publishers, New York, 2000, pp. 29–129, http://dx.doi.org/10.1007/b111467.

[5] R. de Sousa, S. Das Sarma, Theory of nuclear-induced spectral diffusion: Spin decoherence of phosphorus donors in Si and GaAs quantum dots, Phys. Rev. B 68 (2003) 115322, http://dx.doi.org/10.1103/PhysRevB.68.115322, URL https://link.aps.org/doi/10.1103/PhysRevB.68.115322.

[6] W.M. Witzel, S. Das Sarma, Quantum theory for electron spin decoherence induced by nuclear spin dynamics in semiconductor quantum computer architectures: Spectral diffusion of localized electron spins in the nuclear solid-state environment, Phys. Rev. B 74 (2006) 035322, http://dx.doi.org/10.1103/PhysRevB.74.035322, URL https://link.aps.org/doi/10.1103/PhysRevB.74.035322.

[7] W.M. Witzel, S.D. Sarma, Multiple-pulse coherence enhancement of solid state spin qubits, Phys. Rev. Lett. 98 (2007) 077601, http://dx.doi.org/10.1103/PhysRevLett.98.077601, URL https://link.aps.org/doi/10.1103/PhysRevLett.98.077601.

[8] W. Zhang, V.V. Dobrovitski, L. f. Santos, L. Viola, B.N. Harmon, Suppression of electron spin decoherence in a quantum dot, J. Modern Opt. 54 (16–17) (2007) 2629–2640, http://dx.doi.org/10.1080/09500340701534857, arXiv:10.1080/09500340701534857.

[9] S.K. Saikin, W. Yao, L.J. Sham, Single-electron spin decoherence by nuclear spin bath: Linked-cluster expansion approach, Phys. Rev. B 75 (2007) 125314, http://dx.doi.org/10.1103/PhysRevB.75.125314, URL https://link.aps.org/doi/10.1103/PhysRevB.75.125314.

[10] W. Yang, R.-B. Liu, Quantum many-body theory of qubit decoherence in a finite-size spin bath, Phys. Rev. B 78 (2008) 085315, http://dx.doi.org/10.1103/PhysRevB.78.085315, URL https://link.aps.org/doi/10.1103/PhysRevB.78.085315.

[11] W. Yang, R.-B. Liu, Quantum many-body theory of qubit decoherence in a finite-size spin bath. II. Ensemble dynamics, Phys. Rev. B 79 (2009) 115320, http://dx.doi.org/10.1103/PhysRevB.79.115320, URL https://link.aps.org/doi/10.1103/PhysRevB.79.115320.

[12] W. Yang, W.-L. Ma, R.-B. Liu, Quantum many-body theory for electron spin decoherence in nanoscale nuclear spin baths, Rep. Progr. Phys. 80 (1) (2016) 016001, http://dx.doi.org/10.1088/0034-4885/80/1/016001.

[13] G.S. Uhrig, Keeping a quantum bit alive by optimized π-pulse sequences, Phys. Rev. Lett. 98 (10) (2007) 100504, http://dx.doi.org/10.1103/PhysRevLett.98.100504, arXiv:0609203 URL https://link.aps.org/doi/10.1103/PhysRevLett.98.100504.

[14] Ł. Cywiński, R.M. Lutchyn, C.P. Nave, S. Das Sarma, How to enhance dephasing time in superconducting qubits, Phys. Rev. B - Conden. Matter Mater. Phys. 77 (17) (2008) 1–11, http://dx.doi.org/10.1103/PhysRevB.77.174509, arXiv:0712.2225.

[15] J. Bylander, S. Gustavsson, F. Yan, F. Yoshihara, K. Harrabi, G. Fitch, D.G. Cory, Y. Nakamura, J.S. Tsai, W.D. Oliver, Noise spectroscopy through dynamical decoupling with a superconducting flux qubit, Nat. Phys. 7 (7) (2011) 565–570, http://dx.doi.org/10.1038/nphys1994, arXiv:1101.4707.

[16] T. Yuge, S. Sasaki, Y. Hirayama, Measurement of the noise spectrum using a multiple-pulse sequence, Phys. Rev. Lett. 107 (17) (2011) 1–4, http://dx.doi.org/10.1103/PhysRevLett.107.170504, arXiv:1105.1594.

[17] G.A. Álvarez, D. Suter, Measuring the spectrum of colored noise by dynamical decoupling, Phys. Rev. Lett. 107 (23) (2011) 1–5, http://dx.doi.org/10.1103/PhysRevLett.107.230501, arXiv:1106.3463.

[18] P. Szańkowski, G. Ramon, J. Krzywda, D. Kwiatkowski, Ł. Cywiński, Environmental noise spectroscopy with qubits subjected to dynamical decoupling, J. Phys. Condensed Matter 29 (33) (2017) http://dx.doi.org/10.1088/1361-648X/aa7648, arXiv:1705.02262.

[19] W.M. Witzel, K. Young, S. Das Sarma, Converting a real quantum spin bath to an effective classical noise acting on a central spin, Phys. Rev. B 90 (2014) 115431, http://dx.doi.org/10.1103/PhysRevB.90.115431, URL https://link.aps.org/doi/10.1103/PhysRevB.90.115431.

[20] K. Keller, M. Qi, C. Gmeiner, I. Ritsch, A. Godt, G. Jeschke, A. Savitsky, M. Yulikov, Intermolecular background decay in RIDME experiments, Phys. Chem. Chem. Phys. 21 (2019) 8228–8245, http://dx.doi.org/10.1039/C8CP07815G.

[21] S. Kuzin, G. Jeschke, M. Yulikov, Diffusion equation for the longitudinal spectral diffusion: The case of the RIDME experiment, Phys. Chem. Chem. Phys. (2022) http://dx.doi.org/10.1039/D2CP03039J.

[22] J. Soetbeer, M. Hulsmann, A. Godt, Y. Polyhach, G. Jeschke, Dynamical decoupling of nitroxides in o-terphenyl: A study of temperature, deuteration and concentration effects, Phys. Chem. Chem. Phys. 20 (3) (2018) 1615–1628, http://dx.doi.org/10.1039/C7CP07074H.

[23] J. You, D. Carić, B. Rakvin, Z. Štefanić, K. Užarević, M. Kveder, Matrix material structure dependence of the embedded electron spin decoherence, J. Chem. Phys. 150 (16) (2019) 164124, http://dx.doi.org/10.1063/1.5090215, arXiv:10.1063/1.5090215.

[24] M. Kveder, B. Rakvin, J. You, A quantum many body model for the embedded electron spin decoherence in organic solids, J. Chem. Phys. 151 (16) (2019) 164124, http://dx.doi.org/10.1063/1.5124561, arXiv:10.1063/1.5124561.

[25] E.R. Canarie, S.M. Jahn, S. Stoll, Quantitative structure-based prediction of electron spin decoherence in organic radicals, J. Phys. Chem. Lett. 11 (9) (2020) 3396–3400, http://dx.doi.org/10.1021/acs.jpclett.0c00768, PMID: 32282218 arXiv:10.1021/acs.jpclett.0c00768.

[26] G. Horvat, M. Kveder, J. You, Inter-pulse delay optimization for dynamical decoupling pulse sequences with up to six refocusing pulses, Eur. Phys. J. Plus 136 (8) (2021) http://dx.doi.org/10.1140/epjp/s13360-021-01832-y.

[27] J. Soetbeer, M. Millen, K. Zouboulis, M. Hülsmann, A. Godt, Y. Polyhach, G. Jeschke, Dynamical decoupling in water–glycerol glasses: A comparison of nitroxides, trityl radicals and gadolinium complexes, Phys. Chem. Chem. Phys. 23 (9) (2021) 5352–5369, http://dx.doi.org/10.1039/D1CP00055A.

[28] T. Bahrenberg, S.M. Jahn, A. Feintuch, S. Stoll, D. Goldfarb, The decay of the refocused hahn echo in double electron–electron resonance (DEER) experiments, Magn. Res. 2 (1) (2021) 161–173, http://dx.doi.org/10.5194/mr-2-161-2021, URL https://mr.copernicus.org/articles/2/161/2021/.

[29] J. Soetbeer, L.F. Ibáñez, Z. Berkson, Y. Polyhach, G. Jeschke, Regularized dynamical decoupling noise spectroscopy – a decoherence descriptor for radicals in glassy matrices, Phys. Chem. Chem. Phys. 23 (2021) 21664–21676, http://dx.doi.org/10.1039/D1CP03103A.

[30] S.M. Jahn, E.R. Canarie, S. Stoll, Mechanism of electron spin decoherence in a partially deuterated glassy matrix, J. Phys. Chem. Lett. 13 (24) (2022) 5474–5479, http://dx.doi.org/10.1021/acs.jpclett.2c00939, PMID: 35687401 arXiv:10.1021/acs.jpclett.2c00939.

[31] O. Sorensen, G. Eich, M. Levitt, G. Bodenhausen, R. Ernst, Product operator-formalism for the description of NMR pulse experiments, Progr. Nucl. Magn. Reson. Spectrosc. 16 (2) (1983) 163–192.

[32] A. Schweiger, G. Jeschke, Principles of Pulse Electron Paramegnetic Resonance, Oxford University Press, Oxford, 2001.

[33] A. Ponti, A. Schweiger, Echo phenomena in electron paramagnetic resonance spectroscopy, Appl. Magn. Reson. 7 (2–3) (1994) 363–403, http://dx.doi.org/10.1007/BF03162620.

[34] A. Volk, C.J. Kaehler, Density model for aqueous glycerol solutions Andreas, Exp. Fluids 59 (5) (2018) http://dx.doi.org/10.1007/s00348-018-2527-y.

[35] I.V. Blazhnov, N.P. Malomuzh, S.V. Lishchuk, Temperature dependence of density, thermal expansion coefficient and shear viscosity of supercooled glycerol as a reflection of its structure, J. Chem. Phys. 121 (13) (2004) 6435–6441, http://dx.doi.org/10.1063/1.1789474, arXiv:10.1063/1.1789474.

[36] I. Angarita, M.F. Mazzobre, H.R. Corti, M.P. Longinotti, Revisiting the glass transition temperature of water–glycerol mixtures in the bulk and confined in mesoporous silica, Phys. Chem. Chem. Phys. 23 (2021) 17018–17025, http://dx.doi.org/10.1039/D1CP02153B.

[37] B. Doherty, O. Acevedo, OPLS force field for choline chloride-based deep eutectic solvents, J. Phys. Chem. B 122 (43) (2018) 9982–9993, http://dx.doi.org/10.1021/acs.jpcb.8b06647, PMID: 30125108 arXiv:10.1021/acs.jpcb.8b06647.

[38] M.J. Bayro, M. Huber, R. Ramachandran, T.C. Davenport, B.H. Meier, M. Ernst, R.G. Griffin, Dipolar truncation in magic-angle spinning NMR recoupling experiments, J. Chem. Phys. 130 (11) (2009) 114506, http://dx.doi.org/10.1063/1.3089370, arXiv:10.1063/1.3089370.

[39] M. Šimenas, D. Klose, M. Ptak, K. Aidas, M. Mączka, J. Banys, A. Pöppl, G. Jeschke, Magnetic excitation and readout of methyl group tunnel coherence, Sci. Adv. 6 (18) (2020) eaba1517, http://dx.doi.org/10.1126/sciadv.aba1517, arXiv:https://www.science.org/doi/pdf/10.1126/sciadv.aba1517.

[40] G. Jeschke, Rotational coupling in methyl-tunneling electron spin echo envelope modulation, Appl. Magn. Reson. 53 (3-5, SI) (2022) 635–651, http://dx.doi.org/10.1007/s00723-021-01375-6.

[41] N. Wili, H. Hintz, A. Vanas, A. Godt, G. Jeschke, Distance measurement between trityl radicals by pulse dressed electron paramagnetic resonance with phase modulation, Magn. Reson. 1 (1) (2020) 75–87, http://dx.doi.org/10.5194/mr-1-75-2020, URL https://mr.copernicus.org/articles/1/75/2020/.

[42] S. Pronk, S. Páll, R. Schulz, P. Larsson, P. Bjelkmar, R. Apostolov, M.R. Shirts, J.C. Smith, P.M. Kasson, D. van der Spoel, B. Hess, E. Lindahl, GROMACS 4.5: A high-throughput and highly parallel open source molecular simulation toolkit, Bioinformatics 29 (7) (2013) 845–854, http://dx.doi.org/10.1093/bioinformatics/btt055, arXiv:https://academic.oup.com/bioinformatics/article-pdf/29/7/845/17343875/btt055.pdf.

[43] S. Stoll, A. Schweiger, Easyspin, a comprehensive software package for spectral simulation and analysis in EPR, J. Magn. Reson. 178 (1) (2006) 42–55, http://dx.doi.org/10.1016/j.jmr.2005.08.013, URL https://www.sciencedirect.com/science/article/pii/S1090780705002892.